

## Article

# Fiber-Shaped Supercapacitors Fabricated Using Hierarchical Nanostructures of $\text{NiCo}_2\text{O}_4$ Nanoneedles and $\text{MnO}_2$ Nanoflakes on Roughened Ni Wire

Jing Zhang, Prashant S. Shewale and Kwang-Seok Yun \*

Department of Electronic Engineering, Sogang University, 35 Baekbeom-ro, Mapo-gu, Seoul 04107, Korea

\* Correspondence: ksyun@sogang.ac.kr; Tel.: +82-2-705-8915

Received: 8 June 2019; Accepted: 9 August 2019; Published: 14 August 2019



**Abstract:** Electrostatic capacitors have high power density but low energy density. In contrast, batteries and fuel cells have high energy density but low power density. However, supercapacitors can simultaneously achieve both high power density and energy density. Herein, we propose a supercapacitor, in which etched nickel wire was used as a current collector due to its high conductivity. Two redox reactive materials,  $\text{MnO}_2$  nanoflakes and  $\text{NiCo}_2\text{O}_4$  nanoneedles, were used in a hierarchical structure to cover the roughened surface of the Ni wire to maximize the effective surface area. Thus, a specific capacitance, energy density, and power density of  $14.4 \text{ F/cm}^3$ ,  $2 \text{ mWh/cm}^3$ , and  $0.1 \text{ W/cm}^3$ , respectively, was obtained via single-electrode experiments. A fiber-shaped supercapacitor was prepared by twisting two electrodes with solid electrolytes made of KOH and polyvinyl alcohol. Although the solid electrolyte had a low ionic conductivity, the energy density and power density were determined to be  $0.97 \text{ mWh/cm}^3$  and  $49.8 \text{ mW/cm}^3$ , respectively.

**Keywords:** Fiber-shaped supercapacitors; hierarchical nanostructures;  $\text{NiCo}_2\text{O}_4$  nanoneedles;  $\text{MnO}_2$  nanoflakes; flexible supercapacitor

## 1. Introduction

Supercapacitors comprise two current collectors, electrodes, and electrolytes. Supercapacitors can overcome the limitations of energy density in electrostatic capacitors and of power density in Li-ion batteries [1–3]. Supercapacitors can be divided into two categories, electrical double layer capacitors (EDLCs) and pseudo-capacitors.

Significant research has been performed to understand the mechanism of EDLC supercapacitors, using carbon materials such as carbon nanotubes (CNTs), active carbon, and graphene. EDLCs are based on non-faradaic processes where the ions are adsorbed and desorbed physically on the electrode surface without any electron transfer between the electrode and electrolyte. EDLCs are similar to electrostatic capacitors, except that the charges are stored on the electrical double layer, composed of an inner Helmholtz plane (IHP) and the diffuse layer in the bulk electrolyte. Thus, the total capacitance of EDLCs is the sum of the capacitance of the IHP and diffuse layers. The thickness of the adsorbed ions on the electrodes is typically less than 1 nm [1]. When porous, carbon-based materials are used as electrodes for EDLCs, 0.17 to 0.20 electrons can be stored per carbon atom on the surface. Although there is no ion transfer between the electrode and electrolyte interface, electron transfer still occurs from the current collector to the electrode material. Therefore, the conductivity of the electrode and current collector are also important factors in determining the performance. EDLCs have the advantages of high instantaneous output power and long life, but have low energy density [4].

To solve the problems arising from the physical adsorption mechanism and to improve energy density, pseudo-capacitors based on faradaic processes have been proposed. Faradaic processes involve

electron transfer at the interface of the electrode and electrolyte via oxidation and reduction (redox) reactions. In this case, materials with high redox reactivity are used to form electrodes. For example, transition metal oxides, such as  $\text{RuO}_2$ ,  $\text{Co}_3\text{O}_4$ ,  $\text{NiO}$  [5–7], and high conductivity polymers [8,9] are used as electrodes. The reactivity of redox reactions is measured by the number and rate of electrons that can be transferred during the redox reaction. Pseudo-capacitors can have 10 to 100 times higher capacitance than EDLCs. However, the poor conductivity of metal oxides, slow redox reaction processes, and the resultant low power density are the major limitations of pseudo-capacitors [10].

Recently,  $\text{NiCo}_2\text{O}_4$ , a mixed transition metal, was reported to show good performance as an electrode for supercapacitors because of its high conductivity, and high redox activity with hydroxide ions ( $\text{OH}^-$ ) in comparison to other transition metal oxides such as  $\text{RuO}_2$ ,  $\text{Co}_3\text{O}_4$ , and  $\text{NiO}$ . Liang et al. synthesized yolk-shelled  $\text{NiCo}_2\text{O}_4$  spheres and demonstrated a specific capacitance of  $835.7 \text{ F g}^{-1}$  [11]. In addition, Wang et al. successfully synthesized three-dimensional hierarchical structures of  $\text{NiCo}_2\text{O}_4/\text{NiCo}_2\text{O}_4$  core-shell nanocones, which delivered a specific capacitance of  $2045.2 \text{ F g}^{-1}$  [12]. Manganese dioxide ( $\text{MnO}_2$ ) has also been considered as an electrode material owing to its high theoretical specific capacitance of  $1370 \text{ F g}^{-1}$  [13]. The reactive redox reaction, easy synthesis from potassium permanganate ( $\text{KMnO}_4$ ), low cost, and environmental compatibility are some additional advantages of  $\text{MnO}_2$ . However, due to poor electric conductivity ( $10^{-5}$ – $10^{-6} \text{ S cm}^{-1}$ ),  $\text{MnO}_2$  exhibits much lower specific capacitance than the theoretical value [14]. Metal foams such as nickel foam have been widely used in the formation of current collectors to increase the effective surface area. However, metal foam is difficult to utilize in microfabrication [13,15–17].

Microfabrication of energy storage devices is important for micro-scale wearable device applications. These applications require mechanical flexibility and elasticity. To meet these requirements, nanostructured electrodes as thin films have been reported [18–21]. These electrodes were synthesized using materials with high redox activity and exhibited improved energy density and power density. These fiber-shaped supercapacitors provided machinability, breathability, and manufacturing flexibility to woven fabrics for application in textiles [22–24]. In fiber-shaped supercapacitors, the mechanical and electrical properties of current collectors are important in determining the overall performance. Generally, good conductivity, high effective surface area, and mechanical flexibility are required for an efficient current collector. Since carbon nanotubes (CNTs) exhibit high specific capacitance, good conductivity, and large surface areas [25], macro CNT fibers obtained from a CNT cluster can be used to form current collectors [26]. Natural cotton yarn and polymer fibers have also been selected as current collectors for fiber-shaped supercapacitors because of their excellent flexibility. However, additional processes are required to generate conductivity of these materials [27,28]. Recently, Wu et al. synthesized  $\text{NiCo}_2\text{O}_4/\text{MnO}_2$  core-shell nanobrush arrays on carbon fiber to manufacture electrodes for fiber-shaped supercapacitors [29]. The stability and flexibility of this device were shown to be superior, but the device exhibited a moderate specific capacitance of  $1.55 \text{ F cm}^{-2}$ , as the energy density and power density were limited by the small surface area of the electrode and the poor conductivity of the carbon fiber current collector.

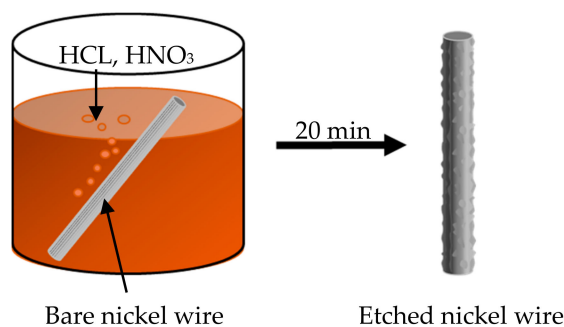
On the basis of previous work, we propose a fiber-shaped supercapacitor with micro-fabricated nanostructures for use as electrodes. In order to increase the surface area of the electrode, hierarchical nanostructures— $\text{NiCo}_2\text{O}_4$  nanoneedles covered with  $\text{MnO}_2$  nanoflakes—were built on etched nickel (Ni) wire. The performance of the  $\text{NiCo}_2\text{O}_4/\text{MnO}_2$  hierarchical nanostructured electrode (HNE) and its super-capacitive performance was thoroughly investigated, and its performance was attributed to a large increase in surface area and the excellent conductivity of the etched Ni current collector.

## 2. Experimental Section

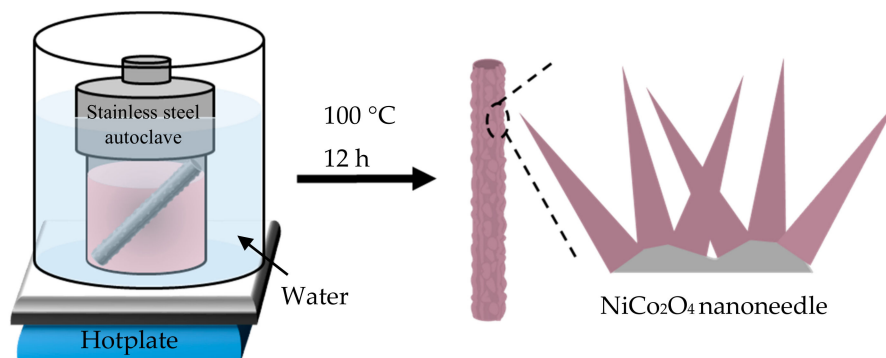
### 2.1. Synthesis of $\text{NiCo}_2\text{O}_4/\text{MnO}_2$ Hierarchical Nanostructures

Figure 1 shows the fabrication processes for  $\text{NiCo}_2\text{O}_4$  nanoneedles on the Ni wire, followed by the growth of  $\text{MnO}_2$  nanoflakes by the formation of hierarchical nanostructures via two separate hydrothermal processes.

#### Step 1: Surface modification



#### Step 2: First hydrothermal synthesis



#### Step 3: Second hydrothermal synthesis

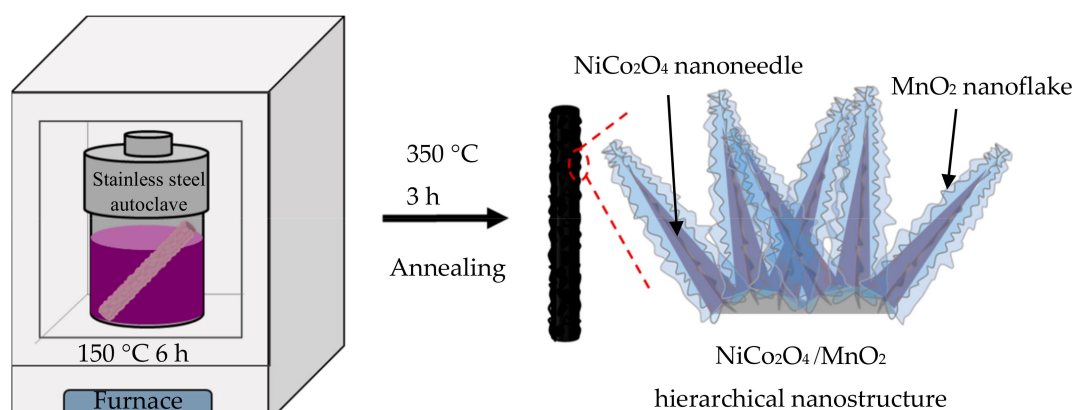


**Figure 1.** Synthesis of  $\text{NiCo}_2\text{O}_4/\text{MnO}_2$  hierarchical nanostructures on etched Ni wire via a two-step hydrothermal method.

Prior to the synthesis of the nanostructures, the surface of the Ni wire (diameter:  $300\text{ }\mu\text{m}$ ) was cleaned and etched with a mixture of hydrochloric acid ( $\text{HCl}$ ) and nitric acid ( $\text{HNO}_3$ ) in the ratio of 4:1 for 20 min. Thereafter, to synthesize  $\text{NiCo}_2\text{O}_4$  nanoneedles on the etched Ni wire surface, 3 mmol nickel

(II) nitrate hexahydrate ( $\text{Ni}(\text{NO}_3)_2 \cdot 6\text{H}_2\text{O}$ ), 6 mmol cobalt (II) nitrate ( $\text{Co}(\text{NO}_3)_2 \cdot 6\text{H}_2\text{O}$ ) and 18 mmol urea ( $\text{CH}_4\text{N}_2\text{O}$ ) were dissolved in 60 mL deionized (DI) water. The etched Ni wire was immersed in a pre-mixed solution and heated for 12 h at 100 °C in a Teflon-lined, stainless steel autoclave. After allowing the solution to cool to room temperature, the sample was cleaned and dried using DI water and an air gun, respectively.

$\text{MnO}_2$  nanoflakes were grown on the  $\text{NiCo}_2\text{O}_4$  nanoneedles. Potassium manganate (VII) ( $\text{KMnO}_4$ ; 1 mmol) was dissolved in 60 mL DI water for the hydrothermal process. Thereafter, the sample was immersed in the solution and was subsequently heated for 6 h at 150 °C. After cleaning with DI water, the sample was annealed for 3 h at 350 °C.

## 2.2. Fabrication of Fiber-Shaped Supercapacitor

In order to construct a fiber-shaped supercapacitor using the etched Ni wires with  $\text{NiCo}_2\text{O}_4/\text{MnO}_2$  hierarchical nanostructures, an electrolyte was first prepared by mixing 10 mL of 2 M potassium hydroxide (KOH), 10 g of polyvinyl alcohol (PVA, Sigma Aldrich), and 100 mL DI water, which were heated for 3 h at 90 °C. Thereafter, the fiber-shaped supercapacitor was fabricated by twisting together the two etched, nanostructure-modified Ni wires after using PVA/KOH gel as an electrolyte as shown in Figure 2.

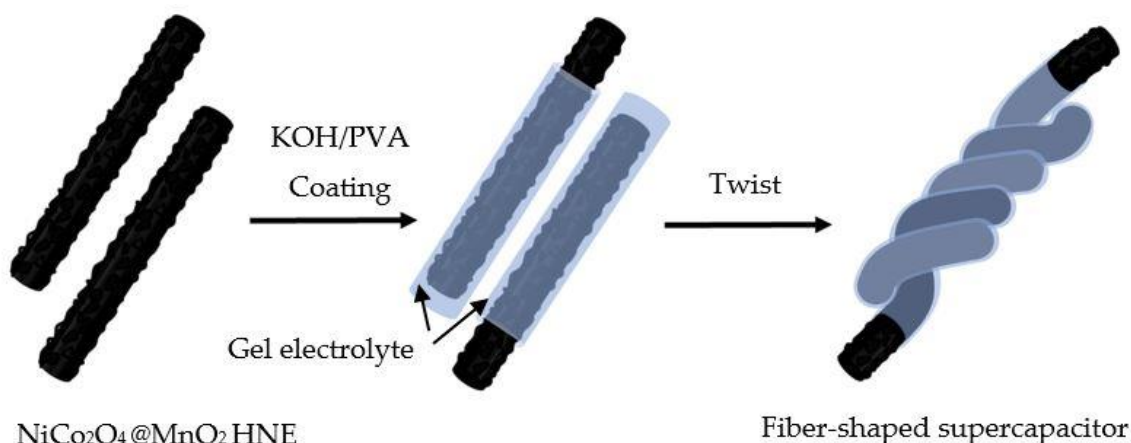
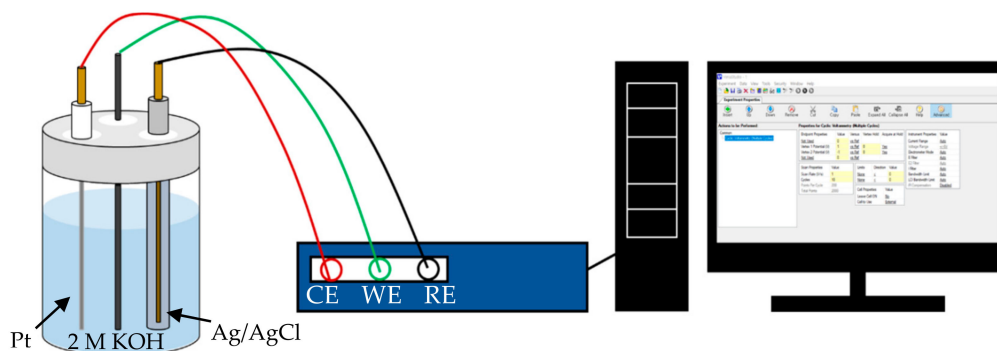


**Figure 2.** The assembly process of the fiber-shaped supercapacitor using KOH/PVA (polyvinyl alcohol) gel electrolyte. HNE: hierarchical nanostructured electrode.

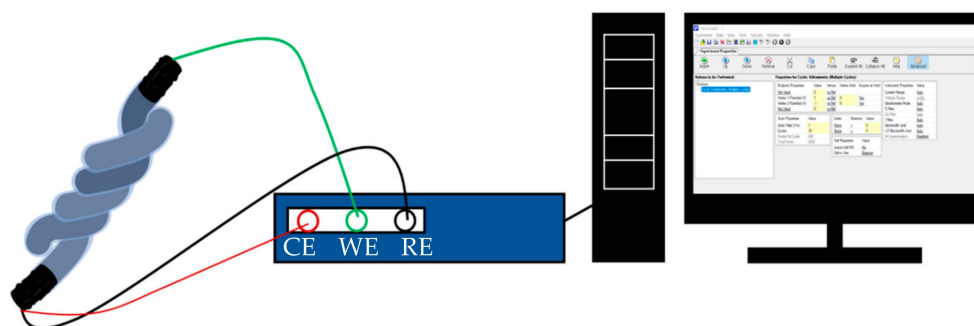
## 2.3. Characterization

The crystal structure and purity of the substrates and the  $\text{NiCo}_2\text{O}_4/\text{MnO}_2$  hierarchical nanostructure were examined by X-ray powder diffraction (XRD) performed on a Bruker D8 Advance X-ray powder diffractometer with  $\text{Cu-K}\alpha$  radiation. Fourier transform infrared (FTIR) spectra were recorded using a spectrophotometer (FTIR-4100, JASCO) at room temperature by KBr pellet technique. X-ray photoelectron spectra (XPS) were used to investigate the element composition through ESCALAB 250 (Thermo Scientific), using an  $\text{Al-K}\alpha$  source. The morphological characteristics of the nanostructures were determined using field emission scanning electron microscopy (FE-SEM, JEM-7100F) at an accelerating voltage of 30 kV. To characterize the electrochemical properties of the samples, cyclic voltammetry (CV) was performed at scan rates from 0.1  $\text{V s}^{-1}$  to 2  $\text{V s}^{-1}$ , galvanostatic charging/discharging (GCD) was performed at currents from 200  $\mu\text{A}$  to 1 mA, and electrochemical impedance spectroscopy (EIS) was performed in the frequency range of 100 kHz to 0.01 Hz using a potentiostat (VersaSTAT 300, Princeton Applied Research, USA) at room temperature. In this work, a single electrode with hierarchical nanostructures was characterized in a three-electrode configuration, as shown in Figure 3a. An Ag/AgCl (in 3M KCl) reference electrode and Pt wire as a counter electrode

in a 2 M KOH solution were utilized to measure the electrochemical performance. The performance of a fiber-shaped supercapacitor was measured via a two-electrode configuration, as shown in Figure 3b.



(a) Three-electrode configuration



(b) Two-electrode configuration

**Figure 3.** Electrochemical set-up of (a) three-electrode and (b) two-electrode configurations.

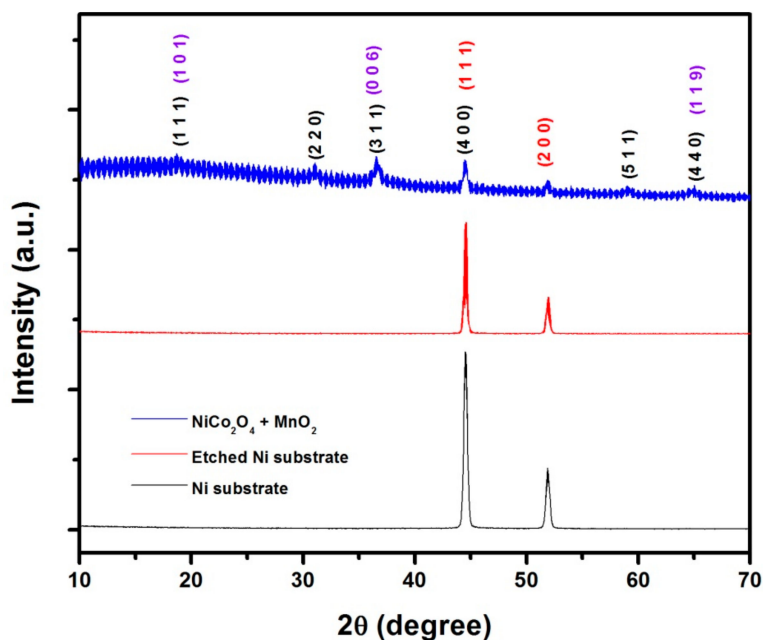
The specific capacitance  $C_v$  was calculated by the equation  $C_v = (I \times t) \div (v \times \Delta V)$  (F/cm<sup>3</sup>); energy density ( $E$ ) was calculated by the equation  $E = C_v \times \Delta V^2 \div 7200$  (Wh/cm<sup>3</sup>); power density ( $P$ ) was calculated by the equation  $P = (E \times 3600) \div t$  (W/cm<sup>3</sup>), where  $I$  is the discharging current,  $t$  is the discharging time,  $v$  is the volume of the electrode, and  $\Delta V$  is the voltage window [30].

### 3. Results and Discussion

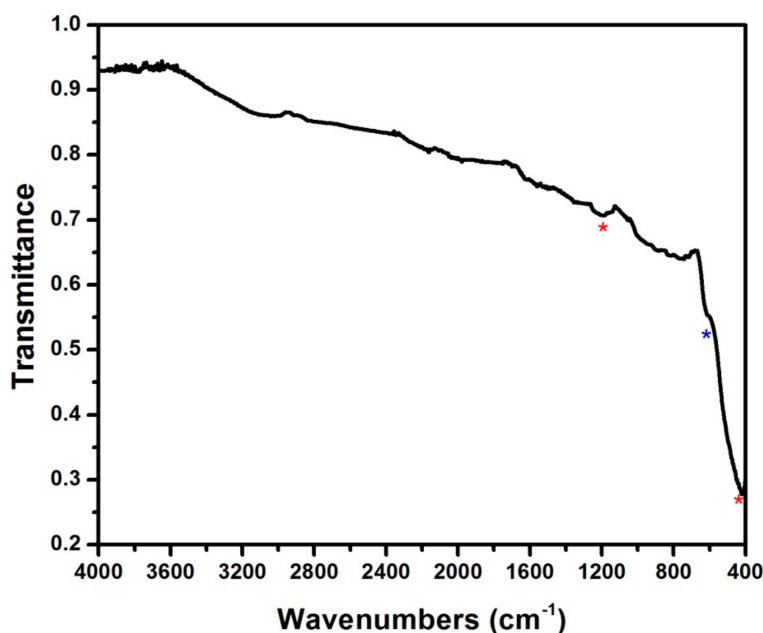
#### 3.1. Structure and Elemental Composition of the Material

Figure 4 shows the X-ray diffraction patterns corresponding to the Ni substrate, etched Ni substrate, and NiCo<sub>2</sub>O<sub>4</sub>/MnO<sub>2</sub> hierarchical nanostructure on etched Ni substrate. Notably, it appears that two of the strongest peaks at  $2\theta = 44.62^\circ$  and  $52^\circ$  for both un-etched and etched Ni substrate were the characteristic (111) and (200) peaks of nickel, and they also appeared in the XRD pattern of the NiCo<sub>2</sub>O<sub>4</sub>/MnO<sub>2</sub> hierarchical nanostructure. Further, the figure also shows the typical XRD pattern of the as-prepared NiCo<sub>2</sub>O<sub>4</sub>/MnO<sub>2</sub> hierarchical nanostructure on etched Ni substrate, in which all diffraction peaks can be assigned to the spinel-structured NiCo<sub>2</sub>O<sub>4</sub> (JCPDS No. 20-0781) and the crystalline birnessite-type MnO<sub>2</sub> (JCPDS card no. 18-0802). The peaks at  $2\theta$  values of  $31^\circ$ ,  $36.8^\circ$ ,  $44.5^\circ$ ,  $58.92^\circ$ , and  $65^\circ$  corresponded to the (220), (311), (400), (511), and (440) crystal faces of NiCo<sub>2</sub>O<sub>4</sub> in its cubic phase. No other impurity peaks appeared, indicating the high purity of the samples. Further, the peak at  $18.7^\circ$  belonged to the (101) plane of the MnO<sub>2</sub> phase, while the peaks at about  $36.8^\circ$  and  $65^\circ$  simultaneously corresponded to both MnO<sub>2</sub> and NiCo<sub>2</sub>O<sub>4</sub>. Moreover, the low and broad diffraction peaks of the NiCo<sub>2</sub>O<sub>4</sub>/MnO<sub>2</sub> hierarchical nanostructure indicated its poor crystallinity, and hence the size of crystallites should be reasonably small [31–33]. Further, Figure 5 shows the FTIR spectrum of

NiCo<sub>2</sub>O<sub>4</sub>/MnO<sub>2</sub> hierarchical nanostructure samples within the wavenumber range of 400 to 4000 cm<sup>-1</sup>. From this result, the weak band at 613 cm<sup>-1</sup> matched the metal–oxygen vibrations of the NiCo<sub>2</sub>O<sub>4</sub> nanoneedles. In addition, two broad bands at 422 cm<sup>-1</sup> and 1191 cm<sup>-1</sup> were observed, corresponding to the characteristic Mn–O stretching vibrations in the MnO<sub>2</sub> crystals. This fact also proves the coexistence of both NiCo<sub>2</sub>O<sub>4</sub> and MnO<sub>2</sub> phases in the NiCo<sub>2</sub>O<sub>4</sub>/MnO<sub>2</sub> hierarchical nanostructure.



**Figure 4.** X-ray diffraction (XRD) patterns of Ni substrate, etched Ni substrate, and the synthesized NiCo<sub>2</sub>O<sub>4</sub>/MnO<sub>2</sub> hierarchical nanostructure.



**Figure 5.** Fourier transform infrared (FTIR) spectrum of the NiCo<sub>2</sub>O<sub>4</sub>/MnO<sub>2</sub> hierarchical nanostructure.

To obtain additional surface information regarding the elemental composition and oxidation states, XPS study on NiCo<sub>2</sub>O<sub>4</sub>/MnO<sub>2</sub> hierarchical nanostructured sample was carried out and the results are shown in Figures 6 and 7. The binding energies of the photoemission peaks in the full XPS survey scan spectrum of the NiCo<sub>2</sub>O<sub>4</sub>/MnO<sub>2</sub> hierarchical nanostructure, shown in Figure 6, confirmed



the presence of Mn, Ni, Co, C, and O elements in the synthesized electrodes. Herein, the C1s peak at 285.06 eV originates from experimental contamination from the pump oil in vacuum system of the XPS instrument. Figure 7a shows the Ni 2p emission spectrum well fitted with two spin-orbit doublets and two shakeup satellites (designated as Sat.), containing a low energy band (Ni 2p<sub>3/2</sub>) and a high energy band (Ni 2p<sub>1/2</sub>) at a binding energy of 855.09 and 872.59 eV, respectively [34,35]. To determine the different oxidation states of the Ni ions, the Mn 2p peak was deconvoluted by Gaussian–Lorentzian function. In the de-convoluted Ni 2p region, the binding energy located at 853.9 and 872.49 eV in Ni 2p<sub>3/2</sub> and Ni 2p<sub>1/2</sub>, respectively, matched the characteristics of Ni<sup>2+</sup>. Additionally, peaks at 857.79 eV in Ni 2p<sub>3/2</sub> and 874.99 eV in Ni 2p<sub>1/2</sub> are ascribed to Ni<sup>3+</sup> oxidation state. The peaks at 861.39 and 880.09 eV, alongside the high binding energy side of the Ni 2p<sub>3/2</sub> and Ni 2p<sub>1/2</sub> edge, are two shakeup satellites. These satellite peaks confirmed that Ni existed largely in Ni<sup>2+</sup> form [36]. Figure 7b shows the Co 2p spectrum fitted into two spin-orbit doublets and satellite peaks, including a low energy band (Co 2p<sub>3/2</sub>) and a high energy band (Co 2p<sub>1/2</sub>) at a binding energy of 780.19 and 795.19 eV, respectively [37]. Furthermore, the deconvolution of the doublet peaks led to the fitting peaks at 780.09 and 795.19 eV, which were attributed to Co<sup>3+</sup>, while the fitted peaks at 781.89 and 797.09 eV were ascribed to Co<sup>2+</sup>. Here, the existence of the majority of Co in the form of the Co<sup>3+</sup> state was exposed by the observed weak satellite peaks [38]. Further, the Mn 2p spectrum in Figure 7c was best fitted with two major peaks, in which the Mn 2p<sub>3/2</sub> peak was centered at 642.19 eV and Mn 2p<sub>1/2</sub> peak at 653.69 eV, indicating that the oxidation state was Mn<sup>4+</sup>, which agrees well with the previous report [39]. The spin–orbit coupling of each peak indicated the presence of Mn<sup>3+</sup> and Mn<sup>4+</sup>, separated by a spin energy of 11.5 eV, and was in good accordance with previous data observed in MnO<sub>2</sub> [40]. The high-resolution spectrum of the O 1s region is shown in Figure 7d, which was distributed into four oxygen contributions (assigned O<sub>1</sub>, O<sub>2</sub>, O<sub>3</sub>, and O<sub>4</sub>). The O<sub>1</sub> component observed at 529.64 eV can be ascribed to a characteristic metal–oxygen bond [41]. The O<sub>2</sub> component apparent at 531.0 eV was related to defects, occurrence of surface species comprising hydroxyls, chemisorbed oxygen, or species intrinsic to the surface of the spinel [42]. The large number of defect sites with low oxygen coordination typically seen in materials with small particles relates to the O<sub>3</sub> component seen at 532.0 eV [43]. Additionally, the O<sub>4</sub> component at 533.04 eV can be accredited to different types of physically and chemically bonded water molecules on top of and inside the electrode material surface [44].

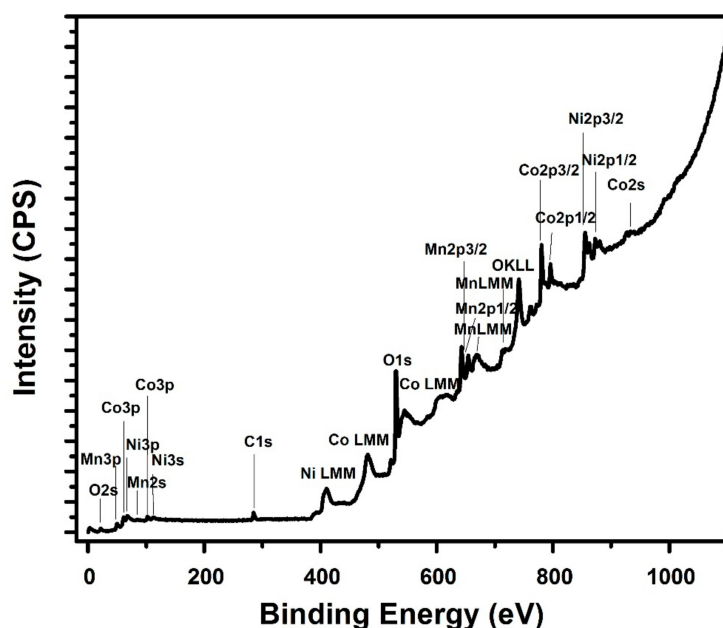


**Figure 6.** X-ray photoelectron spectroscopy (XPS) survey scan spectra of NiCo<sub>2</sub>O<sub>4</sub>/MnO<sub>2</sub> hierarchical nanostructure on etched Ni substrate.

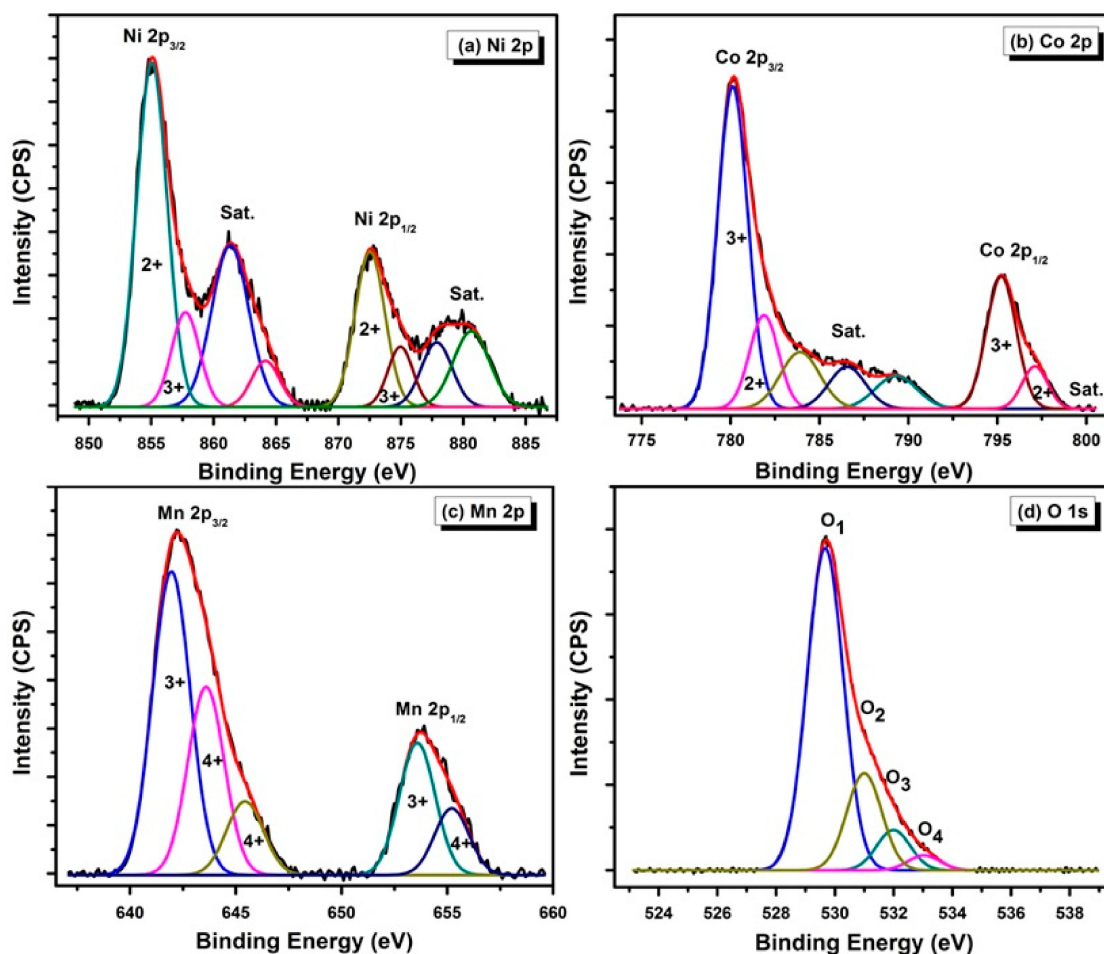


**Figure 7.** (a) High-resolution Ni 2p spectrum; (b) high-resolution Co 2p spectrum; (c) high-resolution Mn 2p spectrum and (d) high-resolution O 1s spectrum.

### 3.2. Fabrication Results

The Ni sample was monitored at each step throughout the synthesis process using scanning electron microscopy (SEM); the images are shown in Figure 8. As shown in Figure 8a, a smooth surface was observed for the Ni wire with a diameter of 300  $\mu\text{m}$ . However, after etching the surface with a mixture of HCl and  $\text{HNO}_3$  for 20 min, the surface became rough and the average diameter was reduced to  $\sim 290 \mu\text{m}$  (Figure 8b). The irregular bumps on the surface effectively increased the reactive surface area. Figure 8c,d shows the Ni wire and a magnified view of the surface after the growth of  $\text{NiCo}_2\text{O}_4$  nanoneedles via the first hydrothermal synthesis. We confirmed that the nanoneedles covered the entire surface of the Ni wire, including the extremely rough microbump structures. The height of the nanoneedles was approximately 1  $\mu\text{m}$ . Figure 8e,f shows the SEM images after the second hydrothermal synthesis. In the magnified view,  $\text{NiCo}_2\text{O}_4/\text{MnO}_2$  hierarchical nanostructures can be observed, in which the entire surface of the  $\text{NiCo}_2\text{O}_4$  nanoneedles was covered with  $\text{MnO}_2$  nanoflakes.



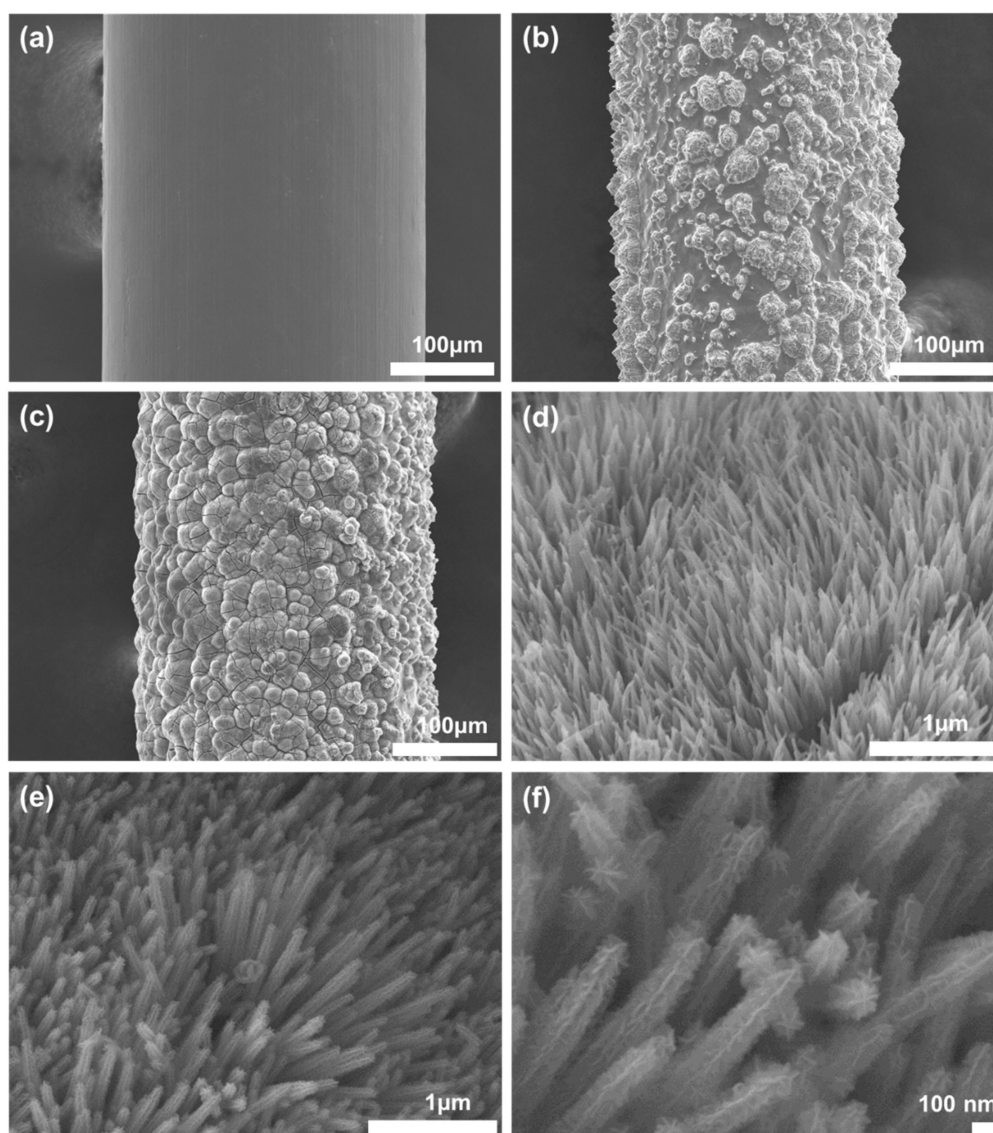


**Figure 8.** (a) Bare Ni wire; (b) etched Ni wire; (c)  $\text{NiCo}_2\text{O}_4/\text{MnO}_2$  hierarchical nanostructures grown on etched Ni wire; (d) magnified view of  $\text{NiCo}_2\text{O}_4$  nanoneedles; (e) and (f) magnified views of  $\text{NiCo}_2\text{O}_4/\text{MnO}_2$  hierarchical nanostructures.

### 3.3. Electrochemical Analysis of Single Electrode

In this work,  $\text{NiCo}_2\text{O}_4$  nanoneedles were synthesized on both smooth and rough Ni wires with bumps on the surface to examine the effect of surface roughness. The materials were tested by CV at a  $0.1 \text{ V s}^{-1}$  scan rate, and GCD at  $200 \mu\text{A}$  charging and discharging current using a three-electrode configuration. As shown in Figure 9, when the  $\text{NiCo}_2\text{O}_4$  nanoneedles were grown on the etched Ni wire surface, the electrochemical performance was better, with large peak current and a long discharging time. These results show that roughening the surface of the electrodes is an efficient way to increase the effective reactive area and subsequently improve the performance. In our experiments, the reduction current increased from  $0.14 \text{ mA}$  to  $0.43 \text{ mA}$  in magnitude (Figure 9a), and the discharging time increased from  $1.5 \text{ s}$  to  $4 \text{ s}$  (Figure 9b).

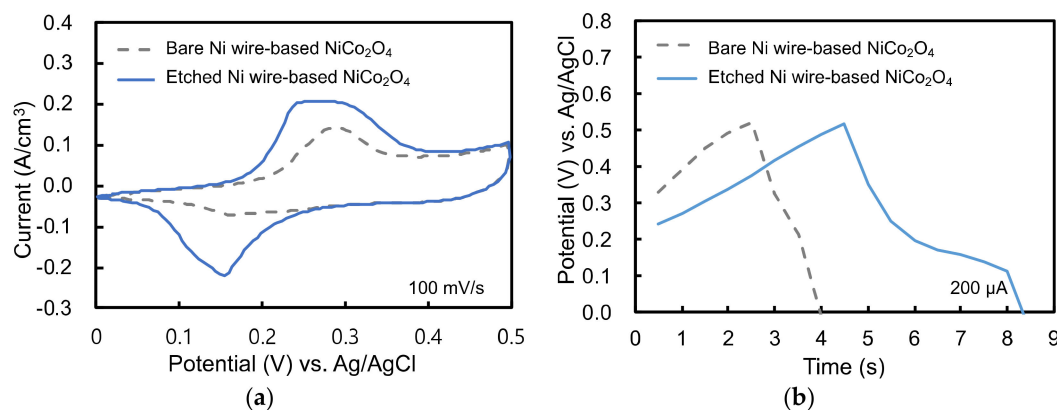


**Figure 9.** (a) Cyclic voltammetry (CV) curve of a bare-Ni-wire-based NiCo<sub>2</sub>O<sub>4</sub> nanoneedle electrode and an etched-Ni-wire-based NiCo<sub>2</sub>O<sub>4</sub> nanoneedle electrode at a 0.1 V s<sup>−1</sup> scan rate; (b) galvanostatic charging/discharging (GCD) curve of the two electrodes at 200  $\mu$ A charging and discharging current.

The electrochemical performance of the electrode with NiCo<sub>2</sub>O<sub>4</sub>/MnO<sub>2</sub> hierarchical nanostructures that were formed via the growth of MnO<sub>2</sub> nanoflakes on the sample, with NiCo<sub>2</sub>O<sub>4</sub> nanoneedles on the etched Ni wire, was also measured as shown in Figure 10. The measurement parameters included 0.1 V s<sup>−1</sup> scan rate and 200  $\mu$ A charging and discharging currents for CV and GCD analysis, respectively. In addition, EIS was performed at a frequency range of 100 kHz to 0.01 Hz under 0.5 V AC voltage in a three-electrode configuration.

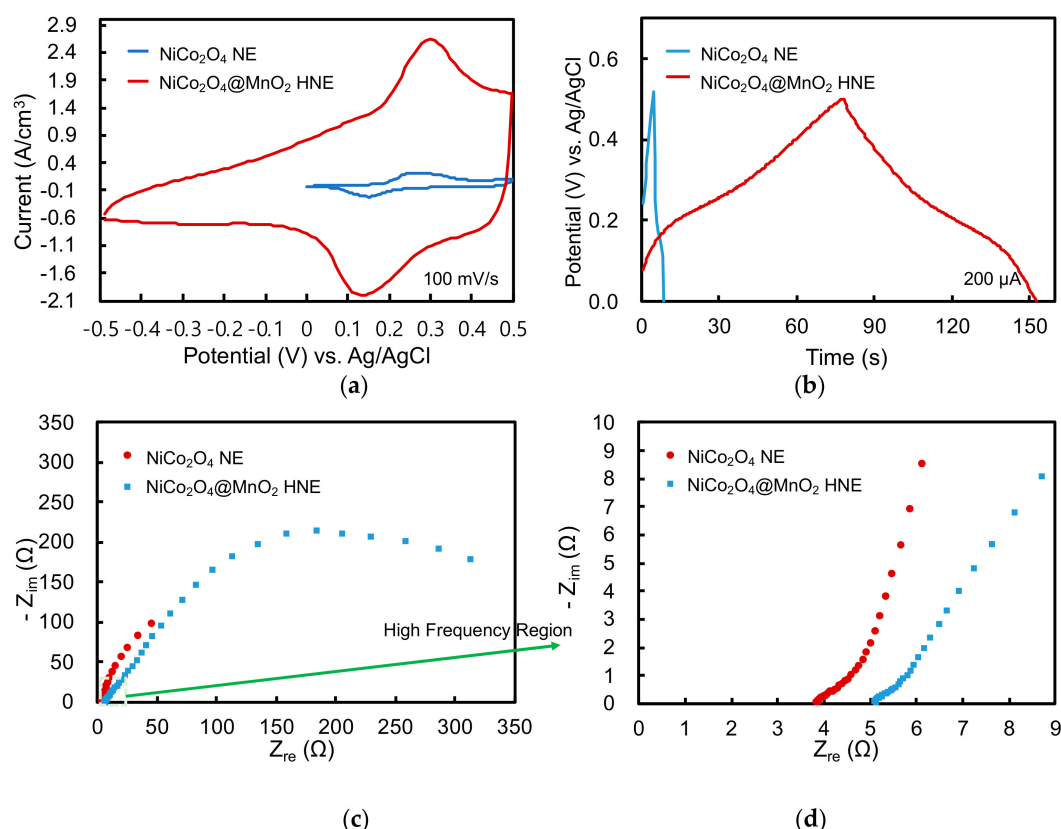


**Figure 10.** (a) The CV curve of an etched-Ni-wire-based NiCo<sub>2</sub>O<sub>4</sub> nanoneedle electrode (NE) and an etched-Ni-wire-based NiCo<sub>2</sub>O<sub>4</sub>/MnO<sub>2</sub> hierarchical nanostructured electrode (HNE) at a 0.1 V s<sup>−1</sup> scan rate; (b) GCD curve of the nanostructured electrodes at 200  $\mu$ A charging and discharging current; electrochemical impedance spectroscopy (EIS) of the nanostructured electrodes at 100 kHz and 0.01 Hz under 0.5 V in the (c) full frequency and (d) high frequency regions.

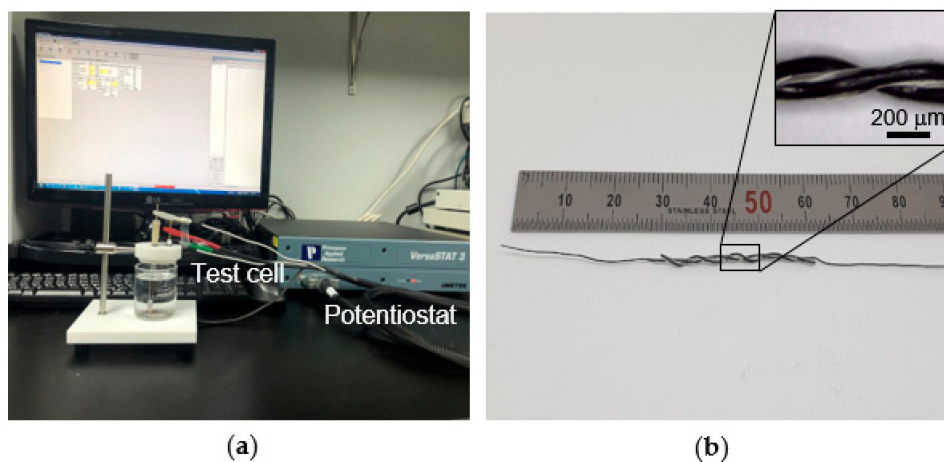
Compared to the  $\text{NiCo}_2\text{O}_4$  nanoneedle electrode (NE) without the  $\text{MnO}_2$  nanoflakes, as shown in the CV experiment in Figure 10a, the  $\text{NiCo}_2\text{O}_4/\text{MnO}_2$  hierarchical nanostructured electrode (HNE) provided a much larger effective surface area to adsorb the  $\text{OH}^-$  ions and react with the  $\text{NiCo}_2\text{O}_4/\text{MnO}_2$ . This structure generated a high peak current via a reversible reaction of  $\text{Co}^{3+}/\text{Co}^{4+}$ ,  $\text{Ni}^{2+}/\text{Ni}^{3+}$ , and  $\text{MnO}_2/\text{Mn}^{2+}$  [45]. The  $\text{NiCo}_2\text{O}_4/\text{MnO}_2$  hierarchical nanostructures showed a much higher electric double layer capacitance in the cyclic voltammetry experiments. By using the  $\text{NiCo}_2\text{O}_4/\text{MnO}_2$  HNE, the peak current improved from 0.43 to 3.97 mA and the voltage window increased by almost a factor of two, from  $-0.5$  V to  $0.5$  V at a  $0.1 \text{ V s}^{-1}$  scan rate. Figure 10b demonstrates that the  $\text{NiCo}_2\text{O}_4/\text{MnO}_2$  HNE possessed a discharge time of 72 s, which was 18 times longer than that of the  $\text{NiCo}_2\text{O}_4$  NE. This extended discharging time was caused not only by the large electric double layer capacitance, but also by an increased redox reaction at the surface. In addition, in this experiment, almost no voltage drop (IR drop) was detected during the current inversion, which implies that the internal resistance was very low [46,47]. The volumetric specific capacitance, energy density, and power density of the  $\text{NiCo}_2\text{O}_4$  NE were  $0.8 \text{ F/cm}^3$  ( $5.93 \text{ mF/cm}^2$ ),  $0.055 \text{ mWh/cm}^3$  ( $0.0004 \text{ mWh/cm}^2$ ) and  $2.75 \text{ mW/cm}^3$  ( $0.02 \text{ mW/cm}^2$ ), respectively. When the results were calculated using the surface area of the electrode, the areal specific capacitance, energy density, and power density became  $5.93 \text{ mF/cm}^2$ ,  $0.0004 \text{ mWh/cm}^2$ , and  $0.02 \text{ mW/cm}^2$ , respectively. For the  $\text{NiCo}_2\text{O}_4/\text{MnO}_2$  HNE, the volumetric specific capacitance, energy density, and power density were  $14.4 \text{ F/cm}^3$ ,  $2 \text{ mWh/cm}^3$ , and  $0.1 \text{ W/cm}^3$ , respectively. The corresponding areal values were  $105.4 \text{ mF/cm}^2$ ,  $0.015 \text{ mWh/cm}^2$ , and  $0.73 \text{ mW/cm}^2$ , respectively.

EIS analysis was used to study the equivalent resistance while supplying  $0.5 \text{ V}$  AC voltage at different frequencies. The Nyquist plot in Figure 10c displays the relationship between the imaginary part ( $Z_{\text{im}}$ ) and the real part ( $Z_{\text{re}}$ ) of the electrode impedance. The initial data point in the high frequency (Figure 10d) measurements shows the initial resistance of the electrode/electrolyte interface, because the effects of mass transfer of the  $\text{OH}^-$  ions on the impedance can be ignored at high frequency [12]. As shown in the magnified view of Figure 10c, the initial resistance was measured as  $5.1 \Omega$  and  $3.87 \Omega$  for the  $\text{NiCo}_2\text{O}_4$  NE and  $\text{NiCo}_2\text{O}_4/\text{MnO}_2$  HNE, respectively. Furthermore, the low frequency measurements reflect that the impedance from mass transfer or ion diffusion was also lower in the  $\text{NiCo}_2\text{O}_4/\text{MnO}_2$  HNE than in the  $\text{NiCo}_2\text{O}_4$  NE.

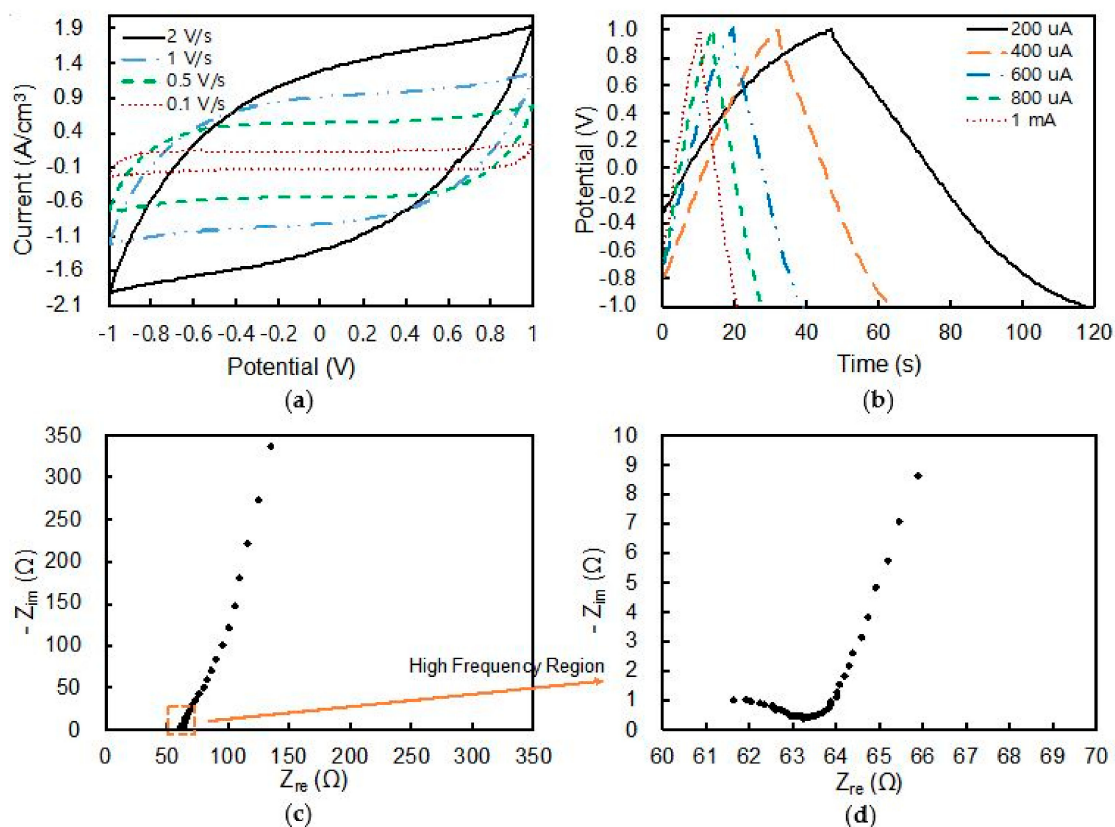
### 3.4. Performance of Fiber-Shaped Supercapacitor

The fiber-shaped supercapacitor comprising the symmetric assembly of two  $\text{NiCo}_2\text{O}_4/\text{MnO}_2$  HNEs, made of etched Ni wires, was characterized as shown in Figure 3b. The experimental setup and fabricated device is shown in Figure 11. The inset of Figure 11b shows a magnified view of the twisted fiber-shaped supercapacitor. The CV curve of the fiber-shaped supercapacitor exhibited a pure capacitive behavior with a rectangular-shaped curve at  $0.1 \text{ V s}^{-1}$  scan rate, as shown in Figure 12a. As the scan rate increased up to  $2 \text{ V s}^{-1}$ , the CV plot became more eye-shaped, since the mobility of  $\text{OH}^-$  ions in the PVA/KOH gel electrolyte was limited and could not match the fast voltage variation at high scan rate. The supercapacitor showed a  $7.58 \text{ mA}$  discharging current at  $2 \text{ V s}^{-1}$ . The GCD was measured at charging and discharging currents ranging from  $200 \mu\text{A}$  to  $1 \text{ mA}$ , and is depicted in Figure 12b. The longest discharging time of  $70 \text{ s}$  was obtained at  $200 \mu\text{A}$ , with a voltage drop of  $0.08 \text{ V}$ . Figure 12c shows the Nyquist plot of the supercapacitor, measured at a frequency from a high value of  $100 \text{ kHz}$  to low value of  $0.01 \text{ Hz}$  at  $2 \text{ V}$  AC voltage. A  $61.4 \Omega$  initial interface resistance was observed between the electrode and electrolyte at high frequency, and the smaller radius of the semicircular plot in the magnified view represents the electron transfer ability, which was slightly decreased during the redox reaction. Additionally, in the low frequency region, the gentle slope shows that ion diffusion is not remarkable. These poor charge transfer characteristics are a limitation of solid-type electrolytes. Nevertheless, compared to previous reports on all solid-state fiber-shaped supercapacitors, our device showed comparable performance for energy density and power density, as shown in Table 1 and in the Ragone plot in Figure 13. In addition, in this work, the GCD was used to check the repeatability of the

cycling performance of the device. After 3000 cycles under a large charging and discharging current of 1 mA, the capacitance retention was kept at 84%, as shown in Figure 14.



**Figure 11.** (a) Experiment set up with potentiostat and (b) photograph of fabricated fiber-shaped supercapacitor. Inset shows the magnified view.

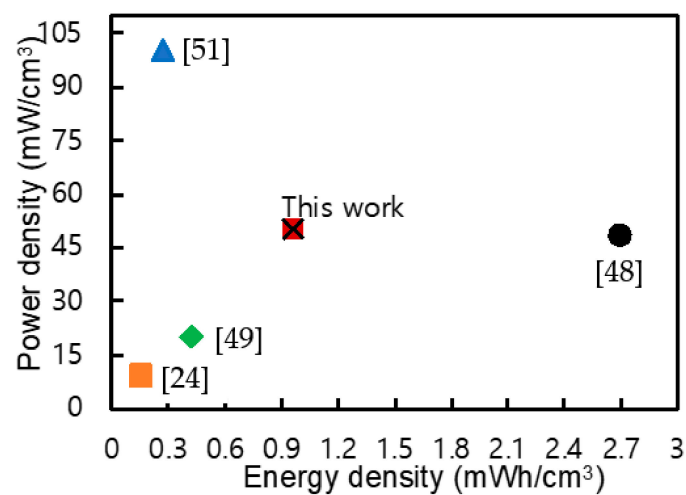
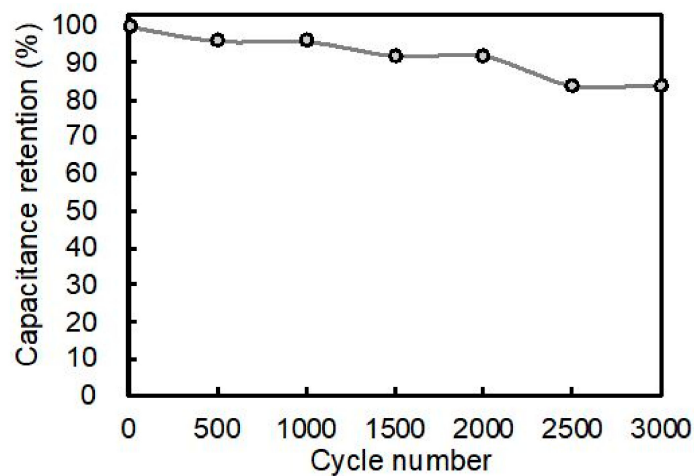


**Figure 12.** (a) CV curve of fiber-shaped supercapacitor at  $0.1 \text{ V s}^{-1}$ – $2 \text{ V s}^{-1}$  scan rate; (b) GCD curve of the nanostructured electrodes at  $200 \text{ μA}$ – $2 \text{ mA}$  charging and discharging currents; (c) and (d) EIS of the nanostructured electrodes at  $100 \text{ kHz}$ – $0.01 \text{ Hz}$  under  $2 \text{ V}$ .



**Table 1.** Comparison of energy density and power density of supercapacitors in recent publications.

Ref.	Device Components	Energy Density	Power Density
[24]	MnO <sub>2</sub> –carbon fiber Fe <sub>2</sub> O <sub>3</sub> –carbon fiber	0.16 mWh/cm <sup>3</sup>	9 mW/cm <sup>3</sup>
[29]	NiCo <sub>2</sub> O <sub>4</sub> /MnO <sub>2</sub> –carbon fiber	1.983 mWh/cm <sup>2</sup>	1.72 mW/cm <sup>2</sup>
[48]	Fe <sub>2</sub> O <sub>3</sub> /NCWs–carbon fiber MnO <sub>2</sub> /TiN–carbon fiber	2.7 mWh/cm <sup>3</sup>	48.6 mW/cm <sup>3</sup>
[49]	MnO <sub>2</sub> /CNT–web paper Fe <sub>2</sub> O <sub>3</sub> –carbon fiber	0.43 mWh/cm <sup>3</sup>	20 mW/cm <sup>3</sup>
[50]	CuCo <sub>2</sub> S <sub>4</sub> –Ni wire	0.007 mWh/cm <sup>2</sup>	0.599 mW/cm <sup>2</sup>
[51]	rGO/MnO <sub>2</sub> –Ni wire	0.27 mWh/cm <sup>3</sup>	100 mW/cm <sup>3</sup>
[52]	Co <sub>3</sub> O <sub>4</sub> –Ni fiber Graphene–carbon fiber	0.62 mWh/cm <sup>3</sup>	1470 mW/cm <sup>3</sup>
[53]	NiO/MnCo–LDH–Ni wire Active carbon–Ni wire	0.0198 mWh/cm <sup>2</sup>	0.38 mW/cm <sup>2</sup>
This work	NiCo <sub>2</sub> O <sub>4</sub> /MnO <sub>2</sub> –roughened Ni wire	0.97 mWh/cm <sup>3</sup>	49.8 mW/cm <sup>3</sup>
		0.007 mWh/cm <sup>2</sup>	0.36 mW/cm <sup>2</sup>

**Figure 13.** Ragone plot of supercapacitors in recent publications.**Figure 14.** Cycling performance of device at charging and discharging current of 1 mA.

#### 4. Conclusions

In summary, NiCo<sub>2</sub>O<sub>4</sub>/MnO<sub>2</sub> hierarchical nanostructures were successfully synthesized on etched Ni wire to create fiber-shaped electrodes for supercapacitors. The phase formation and elemental composition of NiCo<sub>2</sub>O<sub>4</sub>/MnO<sub>2</sub> hierarchical nanostructures were confirmed using XRD, FTIR, and XPS techniques. The samples containing NiCo<sub>2</sub>O<sub>4</sub> nanoneedles covered with MnO<sub>2</sub> nanoflakes had large surface areas. Thus, NiCo<sub>2</sub>O<sub>4</sub>/MnO<sub>2</sub> HNE exhibited a high volumetric specific capacitance of 14.4 F/cm<sup>3</sup>, and areal specific capacitance of 105.4 mF/cm<sup>2</sup>, with an improved volumetric energy density and power density of 2 mWh/cm<sup>3</sup> and 0.1 W/cm<sup>3</sup>, and areal energy density and power density of 0.015 mWh/cm<sup>2</sup> and 0.73 mW/cm<sup>2</sup>, respectively. A fiber-shaped supercapacitor was assembled using two NiCo<sub>2</sub>O<sub>4</sub>/MnO<sub>2</sub> HNEs with a KOH/PVA gel electrolyte, and its performance was demonstrated. Although the supercapacitor suffered from poor ionic conductivity due to the gel electrolyte, our device still showed significantly higher energy density compared to that reported in other recent studies.

**Author Contributions:** The ideas and concept was carried out in collaboration with all authors. J.Z. fabricated this device, carried out the experiments, and wrote this paper; P.S.S. contributed the characterization of materials and prepared the manuscript; K.-S.Y. contributed to the data analysis, the verification of the approach, and reviewed the paper.

**Funding:** This research was supported by Basic Science Research Program through the National Research Foundation of Korea (NRF) funded by the Ministry of Science and ICT (2019R1A2B5B01070298) and Korea Electric Power Corporation (R18XA06-53).

**Conflicts of Interest:** The authors declare no conflict of interest.

#### References

1. Zhao, X.; Sánchez, B.M.; Dobson, P.J.; Grant, P.S. The role of nanomaterials in redox-based supercapacitors for next generation energy storage devices. *Nanoscale* **2011**, *3*, 839–855. [[CrossRef](#)] [[PubMed](#)]
2. Tarascon, J.M. Key challenges in future Li-battery research. *Philos. Trans. R. Soc. A Math. Phys. Eng. Sci.* **2010**, *368*, 3227–3241. [[CrossRef](#)] [[PubMed](#)]
3. Etacheri, V.; Marom, R.; Elazari, R.; Salitra, G.; Aurbach, D. Challenges in the development of advanced Li-ion batteries: A review. *Energy Environ. Sci.* **2011**, *4*, 3243–3262. [[CrossRef](#)]
4. Yang, P.; Mai, W. Flexible solid-state electrochemical supercapacitors. *Nano Energy* **2014**, *8*, 274–290. [[CrossRef](#)]
5. Xia, H.; Meng, Y.S.; Yuan, G.; Cui, C.; Lu, L. A symmetric RuO<sub>2</sub>/RuO<sub>2</sub> supercapacitor operating at 1.6 V by using a neutral aqueous electrolyte. *Electrochem. Solid-State Lett.* **2012**, *15*, A60–A63. [[CrossRef](#)]
6. Xia, X.H.; Tu, J.P.; Mai, Y.J.; Wang, X.L.; Gu, C.D.; Zhao, X.B. Self-supported hydrothermal synthesized hollow Co<sub>3</sub>O<sub>4</sub> nanowire arrays with high supercapacitor capacitance. *J. Mater. Chem.* **2011**, *21*, 9319–9325. [[CrossRef](#)]
7. Lang, J.W.; Kong, L.B.; Wu, W.J.; Luo, Y.C.; Kang, L. Facile approach to prepare loose-packed NiO nano-flakes materials for supercapacitors. *Chem. Commun.* **2008**, *35*, 4213–4215. [[CrossRef](#)]
8. Snook, G.A.; Kao, P.; Best, A.S. Conducting-polymer-based supercapacitor devices and electrodes. *J. Power Sources* **2011**, *196*, 1–12. [[CrossRef](#)]
9. Ryu, K.S.; Kim, K.M.; Park, N.G.; Park, Y.J.; Chang, S.H. Symmetric redox supercapacitor with conducting polyaniline electrodes. *J. Power Sources* **2002**, *103*, 305–309. [[CrossRef](#)]
10. Wang, G.; Zhang, L.; Zhang, J. A review of electrode materials for electrochemical supercapacitors. *Chem. Soc. Rev.* **2012**, *41*, 797–828. [[CrossRef](#)]
11. Wang, L.; Jiao, X.; Liu, P.; Ouyang, Y.; Xia, X.; Lei, W.; Hao, Q. Self-template synthesis of yolk-shelled NiCo<sub>2</sub>O<sub>4</sub> spheres for enhanced hybrid supercapacitors. *Appl. Surf. Sci.* **2018**, *427*, 174–181. [[CrossRef](#)]
12. Wang, X.; Fang, Y.; Shi, B.; Huang, F.; Rong, F.; Que, R. Three-dimensional NiCo<sub>2</sub>O<sub>4</sub>@NiCo<sub>2</sub>O<sub>4</sub> core-shell nanocones arrays for high-performance supercapacitors. *Chem. Eng. J.* **2018**, *344*, 311–319. [[CrossRef](#)]
13. Xu, J.; Sun, Y.; Lu, M.; Wang, L.; Zhang, J.; Qian, J.; Liu, X. Fabrication of hierarchical MnMoO<sub>4</sub>·H<sub>2</sub>O@MnO<sub>2</sub> core-shell nanosheet arrays on nickel foam as an advanced electrode for asymmetric supercapacitors. *Chem. Eng. J.* **2018**, *334*, 1466–1476. [[CrossRef](#)]



14. Xu, K.; Ren, Q.; Liu, Q.; Li, W.; Zou, R.; Hu, J. Design and synthesis of 3D hierarchical NiCo<sub>2</sub>S<sub>4</sub>@MnO<sub>2</sub> core-shell nanosheet arrays for high-performance pseudocapacitors. *Rsc Adv.* **2015**, *5*, 44642–44647. [[CrossRef](#)]
15. Yang, Z.; Zhu, X.; Wang, K.; Ma, G.; Cheng, H.; Xu, F. Preparation of NiCo<sub>2</sub>S<sub>4</sub> flaky arrays on Ni foam as binder-free supercapacitor electrode. *Appl. Surf. Sci.* **2015**, *347*, 690–695. [[CrossRef](#)]
16. Gao, Y.; Chen, S.; Cao, D.; Wang, G.; Yin, J. Electrochemical capacitance of Co<sub>3</sub>O<sub>4</sub> nanowire arrays supported on nickel foam. *J. Power Sources* **2010**, *195*, 1757–1760. [[CrossRef](#)]
17. Xu, J.; Sun, Y.; Lu, M.; Wang, L.; Zhang, J.; Qian, J.; Kim, E.J. Fabrication of porous Mn<sub>2</sub>O<sub>3</sub> microsheet arrays on nickel foam as high-rate electrodes for supercapacitors. *J. Alloy. Compd.* **2017**, *717*, 108–115. [[CrossRef](#)]
18. Kong, W.; Lu, C.; Zhang, W.; Pu, J.; Wang, Z. Homogeneous core-shell NiCo<sub>2</sub>S<sub>4</sub> nanostructures supported on nickel foam for supercapacitors. *J. Mater. Chem. A* **2015**, *3*, 12452–12460. [[CrossRef](#)]
19. Yang, P.; Chao, D.; Zhu, C.; Xia, X.; Zhang, Y.; Wang, X.; Sun, P.; Tay, B.K.; Shen, Z.X.; Mai, W.; et al. Ultrafast-charging supercapacitors based on corn-like titanium nitride nanostructures. *Adv. Sci.* **2016**, *3*, 1500299. [[CrossRef](#)]
20. Zhang, C.; Geng, X.; Tang, S.; Deng, M.; Du, Y. NiCo<sub>2</sub>O<sub>4</sub>@rGO hybrid nanostructures on Ni foam as high-performance supercapacitor electrodes. *J. Mater. Chem. A* **2017**, *5*, 5912–5919. [[CrossRef](#)]
21. Li, J.; Shi, Q.; Shao, Y.; Hou, C.; Li, Y.; Zhang, Q.; Wang, H. Cladding nanostructured AgNWs-MoS<sub>2</sub> electrode material for high-rate and long-life transparent in-plane micro-supercapacitor. *Energy Storage Mater.* **2019**, *16*, 212–219. [[CrossRef](#)]
22. Meng, Y.; Zhao, Y.; Hu, C.; Cheng, H.; Hu, Y.; Zhang, Z.; Shi, G.; Qu, L. All-graphene core-sheath microfibers for all-solid-state, stretchable fibriform supercapacitors and wearable electronic textiles. *Adv. Mater.* **2013**, *25*, 2326–2331. [[CrossRef](#)] [[PubMed](#)]
23. Yang, Y.; Xie, L.; Wen, Z.; Chen, C.; Chen, X.; Wei, A.; Cheng, P.; Xie, X.; Sun, X. Coaxial triboelectric nanogenerator and supercapacitor fiber-based self-charging power fabric. *ACS Appl. Mater. Interfaces* **2018**, *10*, 42356–42362. [[CrossRef](#)] [[PubMed](#)]
24. Cho, S.; Patil, B.; Yu, S.; Ahn, S.; Hwang, J.; Park, C.; Do, K.; Ahn, H. Flexible, Swiss roll, fiber-shaped, asymmetric supercapacitor using MnO<sub>2</sub> and Fe<sub>2</sub>O<sub>3</sub> on carbon fibers. *Electrochim. Acta* **2018**, *269*, 499–508. [[CrossRef](#)]
25. An, K.H.; Kim, W.S.; Park, Y.S.; Choi, Y.C.; Lee, S.M.; Chung, D.C.; Bae, D.J.; Lim, S.C.; Lee, Y.H. Supercapacitors using single-walled carbon nanotube electrodes. *Adv. Mater.* **2001**, *13*, 497–500. [[CrossRef](#)]
26. Xu, P.; Wei, B.; Cao, Z.; Zheng, J.; Gong, K.; Li, F.; Yu, J.; Li, Q.; Lu, W.; Byun, J.H.; et al. Stretchable wire-shaped asymmetric supercapacitors based on pristine and MnO<sub>2</sub> coated carbon nanotube fibers. *ACS Nano* **2015**, *9*, 6088–6096. [[CrossRef](#)]
27. Zhou, Q.; Jia, C.; Ye, X.; Tang, Z.; Wan, Z. A knittable fiber-shaped supercapacitor based on natural cotton thread for wearable electronics. *J. Power Sources* **2016**, *327*, 365–373. [[CrossRef](#)]
28. Qu, G.; Cheng, J.; Li, X.; Yuan, D.; Chen, P.; Chen, X.; Wang, B.; Peng, H. A fiber supercapacitor with high energy density based on hollow graphene/conducting polymer fiber electrode. *Adv. Mater.* **2016**, *28*, 3646–3652. [[CrossRef](#)]
29. Wu, X.; Meng, L.; Wang, Q.; Zhang, W.; Wang, Y. High flexibility and large energy density asymmetric fibered-supercapacitor based on unique NiCo<sub>2</sub>O<sub>4</sub>@MnO<sub>2</sub> core-shell nanobrush arrays electrode. *Electrochim. Acta* **2019**, *295*, 532–539. [[CrossRef](#)]
30. Zhang, Q.; Sun, J.; Pan, Z.; Zhang, J.; Zhao, J.; Wang, X.; Zhang, C.; Yao, Y.; Lu, W.; Li, Q.; et al. Stretchable fiber-shaped asymmetric supercapacitors with ultrahigh energy density. *Nano Energy* **2017**, *39*, 219–228. [[CrossRef](#)]
31. Wu, Z.; Huang, X.-L.; Wang, Z.-L.; Xu, J.-J.; Wang, H.-G.; Zhang, X.-B. Electrostatic Induced Stretch Growth of Homogeneous β-Ni(OH)<sub>2</sub> on Graphene with Enhanced High-Rate Cycling for Supercapacitors. *Sci. Rep.* **2014**, *4*, 1–8. [[CrossRef](#)]
32. Ding, R.; Qi, L.; Wang, H. Porous NiCo<sub>2</sub>O<sub>4</sub> as an anode material for 4.5 V hybrid Li-ion capacitors. *Rsc Adv.* **2013**, *3*, 12581–12584. [[CrossRef](#)]
33. Liu, J.; Liu, C.; Wan, Y.; Liu, W.; Ma, Z.; Ji, S.; Wang, J.; Zhou, Y.; Hodgson, P.; Li, Y. Facile synthesis of NiCo<sub>2</sub>O<sub>4</sub> nanorod arrays on Cu conductive substrates as superior anode materials for high-rate Li-ion batteries. *Cryst. Eng. Commun.* **2013**, *15*, 1578–1585. [[CrossRef](#)]

34. Cui, B.; Lin, H.; Li, Y.Z.; Li, J.B.; Sun, P.; Zhao, X.C.; Liu, C.J. Photophysical and Photocatalytic properties of core-ring structured  $\text{NiCo}_2\text{O}_4$  nanoparticles. *J. Phys. Chem. C* **2009**, *113*, 14083–14087. [[CrossRef](#)]
35. Wu, P.; Cheng, S.; Yao, M.H.; Yang, L.F.; Zhu, Y.Y.; Liu, P.P.; Xing, O.; Zhou, J.; Wang, M.K.; Luo, H.W.; et al. Low-Cost, Self-Standing  $\text{NiCo}_2\text{O}_4$ @CNT/CNT Multilayer Electrode for Flexible Asymmetric Solid-State Supercapacitors. *Adv. Funct. Mater.* **2017**, *27*, 1702160. [[CrossRef](#)]
36. Zhao, B.; Ke, X.K.; Bao, J.H.; Wang, C.L.; Dong, L.; Chen, Y.W.; Chen, H.L. Synthesis of Flower-Like NiO and Effects of Morphology on Its Catalytic Properties. *J. Phys. Chem. C* **2009**, *113*, 14440–14447. [[CrossRef](#)]
37. Xu, K.; Li, W.; Liu, Q.; Li, B.; Liu, X.; An, L.; Chen, Z.; Zou, R.; Hu, J. Hierarchical mesoporous  $\text{NiCo}_2\text{O}_4$ @ $\text{MnO}_2$  core-shell nanowire arrays on nickel foam for aqueous asymmetric supercapacitors. *J. Mater. Chem. A* **2014**, *2*, 4795–4802. [[CrossRef](#)]
38. Fang, C.; Zhang, D.; Cai, S.; Zhang, L.; Huang, L.; Li, H.; Maitarad, P.; Shi, L.; Gao, R.; Zhang, J. Low-temperature selective catalytic reduction of NO with  $\text{NH}_3$  over nanoflaky MnOx on carbon nanotubes in situ prepared via a chemical bath deposition route. *Nanoscale* **2013**, *5*, 9199–9207. [[CrossRef](#)]
39. Toupin, M.; Brousse, T.; Bélanger, D. Charge Storage Mechanism of  $\text{MnO}_2$  Electrode Used in Aqueous Electrochemical Capacitor. *Chem. Mater.* **2004**, *16*, 3184–3190. [[CrossRef](#)]
40. Li, D.; Du, G.; Wang, J.; Guo, Z.; Chen, Z.; Liu, H. Microwave-assisted Synthesis of Flower-like Structure  $\epsilon$ - $\text{MnO}_2$  as Cathode for Lithium Ion Batteries. *J. Chin. Chem. Soc.* **2012**, *59*, 1211–1215. [[CrossRef](#)]
41. Bi, Y.; Nautiyal, A.; Zhang, H.; Luo, J.; Zhang, X. One-pot microwave synthesis of  $\text{NiO}/\text{MnO}_2$  composite as a high-performance electrode material for supercapacitors. *Electrochim. Acta* **2018**, *260*, 952–958. [[CrossRef](#)]
42. Yuan, C.; Li, J.; Hou, L.; Zhang, X.; Shen, L.; Lou, X.W.D. Ultrathin Mesoporous  $\text{NiCo}_2\text{O}_4$  Nanosheets Supported on Ni Foam as Advanced Electrodes for Supercapacitors. *Adv. Funct. Mater.* **2012**, *22*, 4592–4597. [[CrossRef](#)]
43. Jimenez, V.M.; Fernandez, A.; Espinos, J.P.; Gonzalez-Eliphe, A.R. The state of the oxygen at the surface of polycrystalline cobalt oxide. *J. Electron Spectrosc. Relat. Phenom.* **1995**, *71*, 61–71. [[CrossRef](#)]
44. Marco, J.F.; Gancedo, J.R.; Gracia, M.; Gautier, J.L.; Ríos, E.; Berry, F.J. Characterization of the Nickel Cobaltite,  $\text{NiCo}_2\text{O}_4$ , Prepared by Several Methods: An XRD, XANES, EXAFS, and XPS Study. *J. Solid State Chem.* **2000**, *153*, 74–81. [[CrossRef](#)]
45. Li, Y.; Hasin, P.; Wu, Y.  $\text{Ni}_x\text{Co}_{3-x}\text{O}_4$  nanowire arrays for electrocatalytic oxygen evolution. *Adv. Mater.* **2010**, *22*, 1926–1929. [[CrossRef](#)] [[PubMed](#)]
46. Kim, S.K.; Koo, H.J.; Lee, A.; Braun, P.V. Selective Wetting-Induced Micro-Electrode Patterning for Flexible Micro-Supercapacitors. *Adv. Mater.* **2014**, *26*, 5108–5112. [[CrossRef](#)] [[PubMed](#)]
47. Paleo, A.J.; Staiti, P.; Brigandi, A.; Ferreira, F.N.; Rocha, A.M.; Lufrano, F. Supercapacitors based on AC/ $\text{MnO}_2$  deposited onto dip-coated carbon nanofiber cotton fabric electrodes. *Energy Storage Mater.* **2018**, *12*, 204–215. [[CrossRef](#)]
48. Zhang, Y.; Lin, R.; Fu, Y.; Wang, X.; Yu, X.; Li, J.; Zhu, Y.; Tan, S.; Wang, Z. Metal-organic framework derived  $\text{Fe}_2\text{O}_3$  nanocubes on intertwined N-doped carbon nanowires for fiber-shaped supercapacitor. *Mater. Lett.* **2018**, *228*, 9–12. [[CrossRef](#)]
49. Patil, B.; Ahn, S.; Yu, S.; Song, H.; Jeong, Y.; Kim, J.H.; Ahn, H. Electrochemical performance of a coaxial fiber-shaped asymmetric supercapacitor based on nanostructured  $\text{MnO}_2$ /CNT-web paper and  $\text{Fe}_2\text{O}_3$ /carbon fiber electrodes. *Carbon* **2018**, *134*, 366–375. [[CrossRef](#)]
50. Qi, J.; Liu, X.; Sui, Y.; He, Y.; Ren, Y.; Meng, Q.; Wei, F.; Zhang, X. High performance fiber-shaped all-solid-state symmetric supercapacitor based on mesoporous  $\text{CuCo}_2\text{S}_4$  nanosheets. *J. Mater. Sci. Mater. Electron.* **2019**, *30*, 667–676. [[CrossRef](#)]
51. Zhou, J.; Chen, N.; Ge, Y.; Zhu, H.; Feng, X.; Liu, R.; Ma, Y.; Wang, L.; Hou, W. Flexible all-solid-state micro-supercapacitor based on Ni fiber electrode coated with  $\text{MnO}_2$  and reduced graphene oxide via electrochemical deposition. *Sci. China Mater.* **2018**, *61*, 243–253. [[CrossRef](#)]
52. Wang, X.; Liu, B.; Liu, R.; Wang, Q.; Hou, X.; Chen, D.; Wang, R.; Shen, G. Fiber-based flexible all-solid-state asymmetric supercapacitors for integrated photodetecting system. *Angew. Chem. Int. Ed.* **2014**, *53*, 1849–1853. [[CrossRef](#)] [[PubMed](#)]

53. Gao, L.; Fan, R.; Xiao, R.; Cao, K.; Li, P.; Wang, W.; Lu, Y. NiO-bridged MnCo-hydroxides for flexible high-performance fiber-shaped energy storage device. *Appl. Surf. Sci.* **2019**, *475*, 1058–1064. [[CrossRef](#)]



© 2019 by the authors. Licensee MDPI, Basel, Switzerland. This article is an open access article distributed under the terms and conditions of the Creative Commons Attribution (CC BY) license (<http://creativecommons.org/licenses/by/4.0/>).